AJNR

Whole-Brain Vascular Architecture Mapping Identifies Region-Specific Microvascular Profiles in Vivo

Anja Hohmann, Ke Zhang, Christoph M. Mooshage, Johann M.E. Jende, Lukas T. Rotkopf, Heinz-Peter Schlemmer, Martin Bendszus, Wolfgang Wick and Felix T. Kurz

Whole-Brain Vascular Architecture Mapping Identifies Region-Specific Microvascular Profiles in Vivo

Anja Hohmann, Ke Zhang, Christoph M. Mooshage, Johann M.E. Jende, Lukas T. Rotkopf, Heinz-Peter Schlemmer, Martin Bendszus, Wolfgang Wick, and Felix T. Kurz

ABSTRACT

BACKGROUND AND PURPOSE: The novel MR imaging technique of vascular architecture mapping allows in vivo characterization of local changes in cerebral microvasculature, but reference ranges for vascular architecture mapping parameters in healthy brain tissue are lacking, limiting its potential applicability as an MR imaging biomarker in clinical practice. We conducted whole-brain vascular architecture mapping in a large cohort to establish vascular architecture mapping parameter references ranges and identify region-specific cortical and subcortical microvascular profiles.

MATERIALS AND METHODS: This was a single-center examination of adult patients with unifocal, stable low-grade gliomas with multiband spin- and gradient-echo EPI sequence at 3T using parallel imaging. Voxelwise plotting of resulting values for gradient-echo (R_2^*) versus spin-echo (R_2) relaxation rates during contrast agent bolus administration generates vessel vortex curves that allow the extraction of vascular architecture mapping parameters representative of, eg, vessel type, vessel radius, or CBV in the underlying voxel. Averaged whole-brain parametric maps were calculated for 9 parameters, and VOI analysis was conducted on the basis of a standardized brain atlas and individual cortical GM and WM segmentation.

RESULTS: Prevalence of vascular risk factors among subjects ($n = 106$; mean age, 39.2 [SD, 12.5] years; 56 women) was similar to those in the German population. Compared with WM, we found cortical GM to have larger mean vascular calibers (5.80 [SD, 0.59] versus 4.25 [SD, 0.62] $P < .001$), increased blood volume fraction (20.40 [SD, 4.49] s^{-1} versus 11.05 [SD, 2.44] s^{-1}; $P < .001$), and a dominance of venous vessels. Distinct microvascular profiles emerged for cortical GM, where vascular architecture mapping vessel type indicator differed, eg, between the thalamus and cortical GM (mean, -2.47 [SD, 4.02] s^{-2} versus -5.41 [SD, 2.84] s^{-2}; $P < .001$). Intraclass correlation coefficient values indicated overall high test-retest reliability for vascular architecture mapping parameter mean values when comparing multiple scans per subject.

CONCLUSIONS: Whole-brain vascular architecture mapping in the adult brain reveals region-specific microvascular profiles. The obtained parameter reference ranges for distinct anatomic and functional brain areas may be used for future vascular architecture mapping studies on cerebrovascular pathologies and might facilitate early discovery of microvascular changes, in, eg, neurodegeneration and neuro-oncology.

ABBREVIATIONS: BMI = body mass index; BVF = blood volume fraction; CA = contrast agent; CBI = capillary bed identifier; CGI = caliber gradient indicator; cGM = cortical gray matter; CN = caudate nucleus; GE = gradient-echo; GP = globus pallidus; I = maximum distance between the ascending and descending branches of the vascular hysteresis loop; ICC = intraclass correlation coefficient; KPS = Karnofsky Performance Status; MNI = Montreal Neurological Institute; Q = microvessel density parameter; R2 = T2 relaxation rate; rCBV = relative CBV; SAGE = spin-and gradient-echo; SE = spin echo; VAM = vascular architecture mapping; VHL = vascular hysteresis loop; VIPS = vascular-induced bolus peak-time shift; VSI = vessel size index; VTI = vessel type indicator

Microvascular changes play an important role in the pathogenesis of tumors that thrive on microvascular proliferation, as, eg, glioblastoma, but also in the pathophysiology of cardiovascular disease.[1,2] Alterations of cerebral microvessels, such as small-vessel disease, can lead to lacunar infarction and/or dementia.[3] While current methods to describe alterations in the microvasculature mostly rely on imaging methods with a sufficiently high resolution in an ex vivo setting,[4] the translation to clinical, noninvasive in vivo imaging is feasible with dedicated MR images

FIG 1. Flow diagram showing the patient-selection protocol and criteria for inclusion and exclusion. The *asterisk* indicates that multiple scans per patient were used for further subanalyses on intrasubject test-retest reliability. VP-Shunt indicates ventriculoperitoneal shunt.

such as vascular architecture mapping (VAM), also known as vessel architecture imaging.[5,6]

VAM is based on dynamic changes in spin-echo (SE) and gradient-echo (GE) relaxation rates, R2 and R2*, respectively, during the administration of a contrast agent (CA) bolus.[5,7] Due to their different sensitivities to magnetic susceptibility, R2* and R2 are dependent on vascular properties:[8] R2* is more sensitive to both large- and small-caliber vessels, whereas R2 is predominantly sensitive to vessels with diameters smaller than $10\,\mu m$.[5,9] A combined examination of R2 and R2* changes during CA bolus administration, therefore, allows inferring intravoxel vascular arrangements. Depending on the size of in- and outgoing vessels, a time-parametrized plotting of R2* versus R2 generates characteristic vascular hysteresis loops (VHLs).[5,8] Additionally, the shape of the VHL is influenced by a tissue-type dependent temporal shift between GE and SE signals, adding further information about the microvascular and hemodynamic properties in the underlying voxel, such as oxygen saturation differences or flow directions.[5] Parameters derived from VHL, such as their shape, slope, or direction, therefore, provide information about predominant vessel types, their calibers, and arrangement in the underlying voxel, going beyond vessel size imaging.[5,10]

Preliminary studies in humans and animals as well as simulations have shown the potential of VAM as a noninvasive method to describe and monitor microvascular parameters and therapy effects in patients with brain tumors,[5,11] as well as structural changes in patients with dementia[12] or ischemic strokes.[13] Despite its potential as a vascular imaging biomarker, VAM has not yet been translated into wider clinical routine. One limiting factor is that, to date, no comprehensive set of reference values for different anatomic and functional brain regions has been published.

The objective of the present comprehensive study was, therefore, to develop and establish a standardized VAM whole-brain atlas for healthy brain tissue that can serve as a reference for further studies as well as for clinical application. In addition, interactions between different VAM parameters are analyzed, providing further insight into the complex interplay of different microvascular tissue properties.

MATERIALS AND METHODS

Study Design

The local ethics committee of the Medical Faculty of Heidelberg University approved retrospective data evaluation and waived the requirement to obtain informed consent. Subjects were examined on a 3T Magnetom Prisma scanner (Siemens) as part of their regular clinical routine follow-up with a standardized tumor protocol, including FLAIR, diffusion-weighted imaging, T2-weighted imaging, pre- and postcontrast T1-weighted imaging, DSC perfusion and VAM (see also Zhang et al[7]).
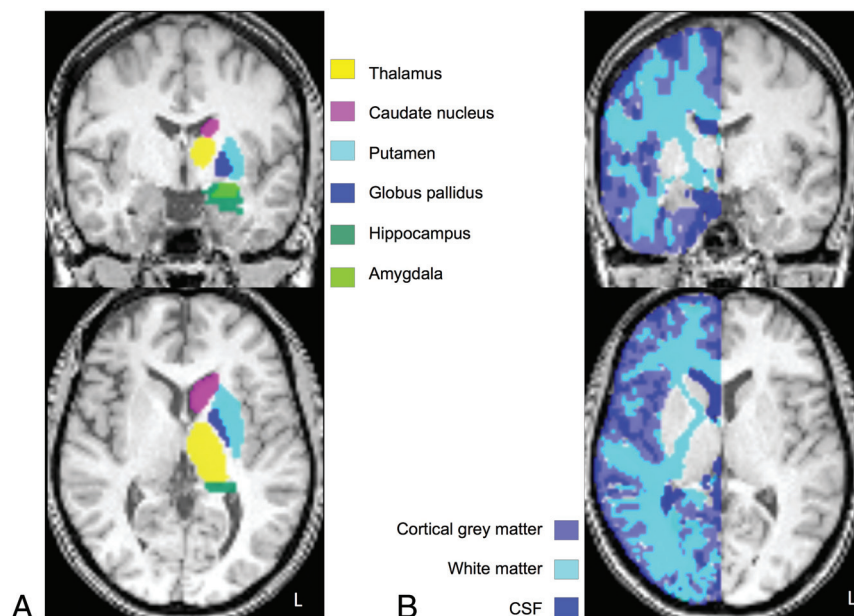
Subjects

Our cohort was selected from an institutional database of consecutive patients with suspected or histologically confirmed World Health Organization grades 1-2 lesions, who were examined between February 2017 and December 2019. Exclusion criteria were the following: younger than 18 years of age, systemic tumor syndromes, neurodevelopmental disorders, diagnosed cerebrovascular disease, and any tumor-specific therapy other than neurosurgical resection before the scan, ie, any previous radio-, chemo, or immunotherapy. Scans with imaging artifacts or tumor mass effects affecting the contralateral, nontumor hemisphere were excluded. Only 1 scan per subject, always the most recent available, and only the nonlesion hemisphere were included in the main analysis. For all subjects who had undergone >1 eligible follow-up scan during the study, the most recent scan available was included into the main analysis, while the first scan available was used for additional intrasubject comparison. A maximum number of 2 scans per subject were included. Patients with infratentorial (mainly cerebellar) lesions were stratified by age group and then randomly allocated to either hemisphere. The patient-selection process is shown in Fig 1.

MR Data Acquisition and VAM

Using multiband accelerated spin- and gradient-echo (SAGE) EPI, we obtained whole-brain VAM in high resolution as described in detail in Zhang et al.[7] Briefly, multiband excitation and blipped controlled aliasing in parallel imaging techniques were applied to track the MR signal changes in both GE and SE contrasts simultaneously. These signals were merged with a phase shift, effectively doubling the readout slices for complete brain coverage following a single contrast agent injection of 0.1-mmol/kg of bodyweight gadoterate meglumine (Dotarem; Guerbet) administered at a rate of 4 mL/s. After CA injection, 60 measurements including 10 baseline measurements, corresponding to 24 slices each with a total brain coverage of 13 cm were acquired using a dual GE/SE readout. Slices were obtained during 90 seconds, with a 15-second baseline acquisition and 75 seconds for gadoterate administration and postgadoterate image acquisition.

Detailed sequence parameters are the following: MR SAGE EPI: TR = 1500 ms, TE (SE) = 90 ms, TE (GE) = 22 ms,

FIG 2. Cerebral volumes of interest. Axial representation of VOIs on spatially normalized T1-weighted images displaying 6 atlas-based anatomic VOIs (female subject, 27 years of age; right-sided lesion) (*A*) and individually segmented gray and white matter VOIs (female subject, 38 years of age; left-sided lesion) (*B*). Only the hemisphere contralateral to the lesion was analyzed for each subject, with a total of 8 VOIs per subject.

interslice gap = 0.9 mm, section thickness = 4.5 mm, voxel size = $2 \times 2 \times 5.4$ mm^3, matrix dimensions = 120×120, multiband factor = 2, in-plane acceleration factor = 3, echo-train length = 20 ms, acquisition time = 1.5 minutes; 3D T1-weighted image MPRAGE sequence for high-resolution anatomic images: TR = 1790 ms, TE = 3.7 ms, flip angle = 15°, section thickness = 1 mm, field of view = 250×250 mm^2, voxel size = $0.78 \times 0.78 \times 1$ mm^3; and DSC MR perfusion: TR = 2220 ms, TE = 37 ms, flip angle = 90°, FOV = 240×240 mm^2, during CA administration (0.1-mmol/kg of bodyweight gadoterate meglumine at 4 mL/s.).

Data Postprocessing

Analysis of VAM was performed using a custom-built code in Matlab R2020a (MathWorks). Following motion correction in SPM12 (http://www.fil.ion.ucl.ac.uk/spm/software/spm12), relaxation rates were calculated from the observed signal intensities S(t), during contrast bolus administration, and average baseline signal intensity, S_0, as $\Delta R(t) = -\frac{1}{TE}\ln\left(\frac{S(t)}{S_0}\right)$, for SE and GE relaxation rates, respectively. Voxels with peak signal (p_s) greater than 2 times the sum of averaged baseline signal (μ) and baseline SD (σ), ie, $p_s > 2[\mu + \sigma]$, were included in the following analysis. Any remaining voxels were excluded. To account for contrast agent leakage effects, we applied the correction method proposed by Boxerman et al.[14] To calculate the $\Delta R(t)_{2,SE}$ versus $\Delta R(t)_{2,GE}$ diagram, we fitted the corrected relaxation rate time curves using a gamma variate function.[15] The fitting process used nonlinear least squares with a maximum of 4000 iterations. Fits with an *r* value < 0.35 were excluded from the analysis; in case of fitting errors, the signal was set to zero. Plotting the $\Delta R(t)_{2,SE}$ versus $\Delta R(t)_{2,GE}$ diagram generated a VHL as described in Emblem et

al[5] and Zhang et al.[7] Calculation of vessel size index (VSI) and microvessel density parameter Q were based on the method by Xu et al.[16]

From the VHL, 6 parameters were extracted, as described by Zhang et al:[7] vessel type indicator (VTI) as the area of the VHL, and parameter I as the maximum distance between the ascending and descending branches of the VHL. Values for both parameters I and VTI were signed according to the direction of the loop—with positive values, if the VHL transversed clockwise, and negative values for a counter-clockwise direction. We further computed the VHL long axis, defined as a linear fit of the VHL, and the short axis, perpendicular to the long axis. The length of the short axis was called parameter capillary bed identifier (CBI) because it has been shown to identify capillary beds, ie, local minima of both oxygen saturation and vessel caliber. The length of the long axis was abbreviated blood volume fraction (BVF) because it correlates with the CBV fraction.[5,7] Its slope was called the caliber gradient indicator (CGI), indicating both oxygen saturation levels and vessel caliber,[5,8] with higher values associated with large venule-like vessels.

We calculated vascular-induced bolus peak-time shift (VIPS), a parameter that correlates with blood flow velocity,[17] from the temporal shift between the time-to-peak of the SE and GE EPI signal curves. Finally, relative cerebral blood volume (rCBV) was computed from the DSC perfusion sequence as in Buschle et al.[9]

Eventually, 9 whole-brain VAM parameter maps were calculated for each scan. For visualization, the hemisphere with the lesion was set to null, resulting in half-brain maps for each subject.

VOI Analysis

Subjects' high-resolution T1-weighted anatomic images were coregistered to their VAM parameter maps. Spatial normalization to standard Montreal Neurological Institute (MNI) space was performed with tissue probability maps using mutual information affine registration in SPM12.[18] Subsequently, the individual transformation parameters were applied to spatially normalize all tissue segmentations and VAM maps for each subject.

VOIs were selected from the automated anatomical labeling atlas 3 (AAL3)[19] for the right and left caudate nucleus (CN), thalamus, putamen, globus pallidus (GP), hippocampus, and amygdala (Fig 2*A*). For each subject, cortical gray matter (cGM) and supratentorial WM VOIs were individually delineated using automated tissue segmentation in FSL FAST[20] (https://poc.vl-e.nl/distribution/manual/fsl-3.2/fast/index.html) on coregistered T1 images, with subsequent subtraction of both the infratentorial region and subcortical GM (Fig 2*B*).

VOIs were checked visually by a trained neuroradiologist with >10 years of clinical experience and a neurologist with 6 years of neurologic imaging experience. Eight VOIs per subject were analyzed.

Statistical Analysis

Statistical analyses were conducted in GraphPad Prism7 (GraphPad Software) and Matlab R2020a. Values are reported as mean value per VOI for each subject. The level of significance was set at $P < .05$ for all tests. Gaussian normal distribution was assessed by the D'Agostino-Pearson omnibus normality test. If data followed a Gaussian normal distribution, t tests were used for comparisons between the 2 groups and 1-way ANOVAs were used for comparisons between >2 groups. Otherwise, Mann-Whitney, respectively, Kruskal-Wallis tests were used. We corrected for multiple comparisons using the post hoc Dunn correction. Correlation analysis was performed by using the Spearman rank correlation, with controlling for age and body mass index (BMI).[21] In a subgroup of patients, test-retest reliability was assessed by calculating intraclass correlation

coefficients (ICC) for mean values between 2 consecutive scans per subject. ICC estimates and their 95% confident intervals were calculated using Matlab based on a single-rating, absolute-agreement, 2-way mixed-effects model.[22]

RESULTS

In total, 106 scans (53 left hemispheres, 53 right hemispheres) were included in the main analysis. No significant difference was found for age, sex, Karnofsky Performance Status (KPS), BMI, or number of cardiovascular risk factors between hemisphere groups; therefore, subsequent processing of VOIs was performed across hemispheres.

Demographics

We examined 106 individual subjects (56 women; mean age, 39.2 years; range, 20–70 years), with an average KPS of 95.2. Cardiovascular risk factor prevalence was similar to the nationwide averages in Germany[23] (Table 1). Twenty-seven subjects (13 women) had undergone >1 eligible follow-up scan, of which we included a maximum number of 2 scans per subject into a subanalysis. The mean time difference between these 2 scans was 13.5 (SD, 6.88) months, with subjects' mean age at acquisition 36.5 (SD, 11.4) years (scan 1) and 37.8 (SD, 11.3) years (scan 2).

VAM Parametric Maps

Mean values ($n = 106$) were calculated for all 9 imaging parameters for each of the 8 VOIs (Table 2). Whole-brain parametric maps were generated for each VAM parameter by averaging the spatially normalized, healthy hemispheres across scans ($n = 53$ left, $n = 53$ right), while subtracting the brainstem and cerebellum region in the infratentorial tumor subgroup ($n = 24$). For visualization purposes, both averaged hemispheres were joined together as 1 image. Axial representations of spatially normalized, averaged parameters I, VTI, and CBI in MNI standard

Table 1: Demographics and distribution of individual vascular risk factors within the cohort ($n = 106$)[a]

| Variable	Cohort
Age (mean) (range) (yr)	39.2 (SD, 12.5) (20–70)
Sex (% female)	52.8
BMI (mean) (range) (kg/m^2)	25.7 (SD, 4.2) (18.4–37.7)
Vascular risk factors (No.) (% of 106)	
Obesity (BMI >30)	19 (17.9%)
Arterial hypertension	16 (15.1%)
Diabetes mellitus type 2	4 (3.8%)
Smoking	25 (23.6%)
KPS (mean) (range)	95.2 (SD, 6.8) (80–100)

[a] Data are displayed as mean values (SD) and (range) except where otherwise indicated.

Table 2: VAM parameter value ranges within cerebral VOIs[a]

Mean [95% CI]	Cortical GM	CN	Thalamus	Putamen	GP	Hippocampus	Amygdala	WM
Average mask size (voxel)	38,354	833	1107	1031	287	939	234	36,322
I	−2.27	−2.42	−1.06	−1.89	−0.95	−2.39	−1.79	−1.33
[s^{-1}]	[−2.45 to −2.08]	[−2.79 to −2.04]	[−1.37 to −0.75]	[−2.11 to −1.67]	[−1.23 to −0.67]	[−2.69 to −2.09]	[−2.31 to −1.26]	[−1.44 to −1.22]
VTI	−5.41	−5.66	−2.47	−3.64	−2.81	−6.60	−5.13	−2.60
[s^{-2}]	[−5.96 to −4.86]	[−6.58 to −4.75]	[−.25 to −1.7]	[−4.24 to −3.04]	[−3.81 to −1.82]	[−7.5 to −5.7]	[−7.23 to −3.02]	[−2.84 to −2.35]
CBI	1.44	1.34	1.73	1.63	2.46	1.65	2.17	1.16
[s^{-1}]	[1.38–1.49]	[1.28–1.4]	[1.67–1.79]	[1.57–1.7]	[2.36–2.56]	[1.6–1.71]	[2.08–2.27]	[1.12–1.19]
BVF	20.40	16.39	18.28	15.52	15.60	22.05	23.92	11.05
[s^{-1}]	[19.53–21.26]	[15.63–17.15]	[17.46–19.1]	[14.7–16.33]	[14.88–16.32]	[21.1–22.99]	[22.67–25.16]	[10.58–11.52]
VIPS	−3.97	−2.82	0.02	−2.23	6.68	−5.39	−7.17	−3.19
[10^{-1} s]	[−4.34 to −3.60]	[−4.25 to −1.38]	[−0.75 to 0.79]	[−2.84 to −1.61]	[4.91–8.44]	[−6.29 to −4.49]	[−8.89 to −5.46]	[−3.64 to −2.74]
rCBV	3.03	2.44	2.79	1.97	1.80	4.20	4.16	1.61
[10^{-2}]	[3.01–3.05]	[2.37–2.51]	[2.69–2.88]	[1.93–2.02]	[1.74–1.85]	[4.07–4.34]	[3.95–4.36]	[1.58–1.63]
VSI	37.32	43.20	29.11	12.93	10.93	45.20	45.25	19.29
[μm]	[36.43–38.22]	[40.2–46.2]	[27.31–30.91]	[12.53–13.32]	[10.13–11.73]	[43.3–47.1]	[42.37–48.13]	[18.85–19.74]
Q	4.25	3.36	4.50	4.91	5.90	3.81	3.90	4.23
[10$^{-2} \cdot$ms$^{-1/3}$]	[4.20–4.30]	[3.24–3.48]	[4.42–4.57]	[4.85–4.97]	[5.75–6.05]	[3.74–3.88]	[3.8–4]	[4.18–4.27]
CGI	5.80	6.19	5.10	4.14	3.14	6.10	5.68	4.25
[ ]	[5.68–5.91]	[5.96–6.42]	[4.91–5.28]	[4.01–4.28]	[2.99–3.29]	[5.93–6.26]	[5.47–5.89]	[4.13–4.36]

Note:—[ ] indicates 95% confidence intervals.
[a] Data are presented as mean values with 95% confidence intervals for mean values.
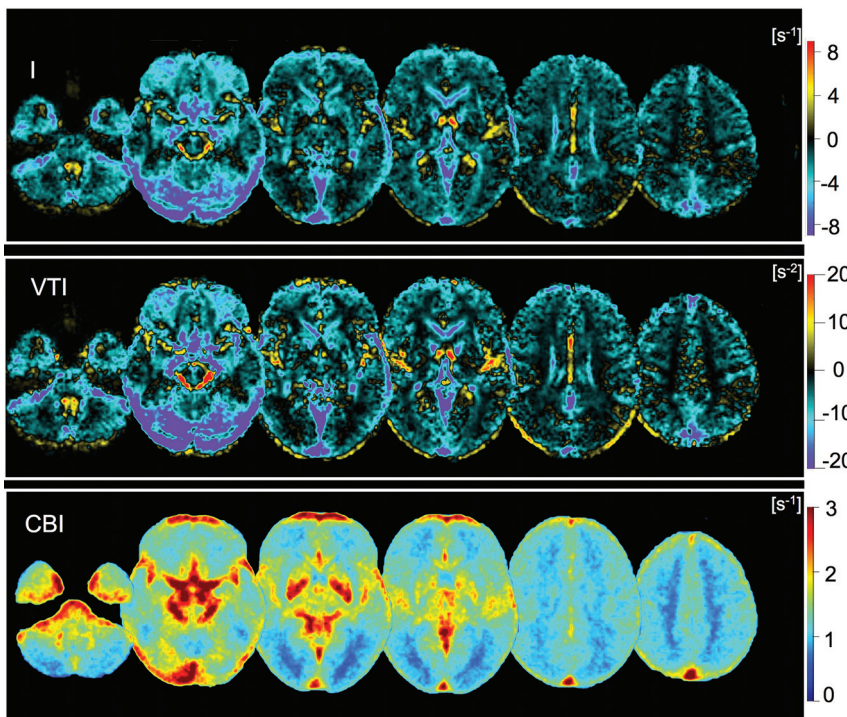
FIG 3. Color representations of distance map parameters I, VTI, and CBI. Parameters I, VTI, and CBI are shown as spatially normalized, averaged axial parametric maps. In MNI standard space, slice coordinates are as follows for all maps (from left to right, Z-axis): -40, -14, 0, 8, 24, 44. Maps of parameters I and VTI are closely correlated and depict differences between brain regions with predominantly venous outflow, eg, close to the transverse and rectus sinus, and predominantly arterial inflow, eg, in the insular cortex. Parameter CBI contrasts brain regions with increased capillary vascularization, such as the GP and hippocampus.

space are shown in Fig 3, for BVF, VIPS, and rCBV in Fig 4, and for VSI, Q, and CGI in Fig 5.

Microvasculature Profiles for Cortical GM and WM
Signed parameters VTI and I showed negative values for all examined VOIs, indicating an overall predominance of capillaries and venules in healthy brain tissue. cGM exhibited higher negative values compared with WM for parameter I (-2.27 [SD, 0.97] s^{-1} versus -1.33 [SD, 0.56] s^{-1}, $P < .001$) and VTI (-5.41 [SD, 2.84] s^{-2} versus -2.60 [SD, 1.29] s^{-2}, $P < .001$).

Additionally, cGM voxels contained vessels with larger calibers compared with WM, both when measured with VSI (37.32 [SD, 4.65] μm versus 19.29 [SD, 2.32] μm, $P < .001$) and CGI (5.80 [SD, 0.59] versus 4.25 [SD, 0.62] (unitless), $P < .001$). Compared with WM, cGM voxels had a higher BVF (20.40 [SD, 4.49] s^{-1} versus 11.05 [SD, 2.44] s^{-1}, $P < .001$) and higher rCBV (3.03 [SD, 0.11]$\cdot 10^{-2}$ versus 1.61 [SD, 0.11]$\cdot 10^{-2}$, $P < .001$).

CBI values were lower in WM (cGM: 1.44 [SD, 0.28] s^{-1}; WM: 1.16 [SD, 0.19] s^{-1}, $P < .001$), indicating a lower difference in oxygen saturation between vessels. No difference was found between GM and WM for microvessel density Q and parameter VIPS (Table 2).

Gray and White Matter-like Profiles in Subcortical GM
Further comparisons revealed distinct microvasculature patterns between cortical and different subcortical GM areas. Absolute

VTI values in the putamen (-3.64 [SD, 3.11] s^{-2}), GP (-2.81 [SD, 5.17] s^{-2}), and thalamus (-2.47 [SD, 4.02] s^{-2}) were lower than in those in the cGM (all $P < .01$) but did not differ from WM (all $P > .05$). VTI in the CN did not differ from cGM ($P = .99$), but from WM and the other basal ganglia (all $P < .05$). Furthermore, absolute VTI values in the hippocampus and amygdala did not differ from those in the cGM or CN (all $P > .05$) but were higher than WM values (both $P < .05$). Other VAM parameters did not significantly differ between the hippocampus and amygdala.

For parameters CGI, VIPS, and VSI, compared with cGM, mean values were lower or less negative for each of the subcortical nuclei (putamen, GP, thalamus, all $P < .05$) apart from the CN, but no difference was found between the CN and cGM (all $P > .05$).

However, BVF and rCBV, measuring CBV, were significantly lower in the CN than in cGM (both $P < .001$) (Table 2). The GP and putamen exhibited lower BVF (GP: 15.60 [SD, 3.73] s^{-1}; putamen: 15.52 [SD, 4.24] s^{-1}) and lower rCBV (GP: 1.80 [SD, 0.29] 10^{-2}; putamen: 1.97 [SD, 0.25] 10^{-2}) than cGM as well (all $P < .001$), while there was no difference in CBV between the thalamus and cGM.

Further analysis showed that putamen and GP differed significantly in I, CGI, and Q. BVF did not differ between the subcortical GM nuclei (all $P > .05$).

The highest values for VIPS, a parameter indicating blood flow velocity and therefore vessel type, were observed in the GP (6.68 [SD, 9.18] 10^{-1} s, comparisons with all other VOIs: all $P < .05$), followed by the thalamus (0.02 [SD, 4.00] 10^{-1} s, all $P < .05$). Microvessel density Q was highest in the GP (all $P < .05$), followed by the putamen (all $P < .05$) and thalamus (4.50 [SD, 0.39] $10^{-2} \cdot ms^{-1/3}$, comparisons with all other VOIs except cGM: $P < .05$). Q did not differ between the cGM and thalamus ($P = .10$).

Test-Retest Reliability and Value Validation
Overall, test-retest reliability was high for VAM parameters, with ICC values indicating moderate-to-excellent agreement between 2 separate scans in a subset of subjects ($n = 27$) (Table 3). Only signed parameters I (ICC = 0.49) and VTI (ICC = 0.36) showed poor test-retest reliability in our sample. When analyzing each VOI separately, we found agreement to be poor only for mean values from very small VOIs, ie, the amygdala (234 voxels) and GP (287 voxels) for both I and VTI. Excluding these 2 VOIs from analysis yielded ICC values indicative of moderate-to-good agreement between scans (ICC = 0.64 for I; ICC = 0.66 for
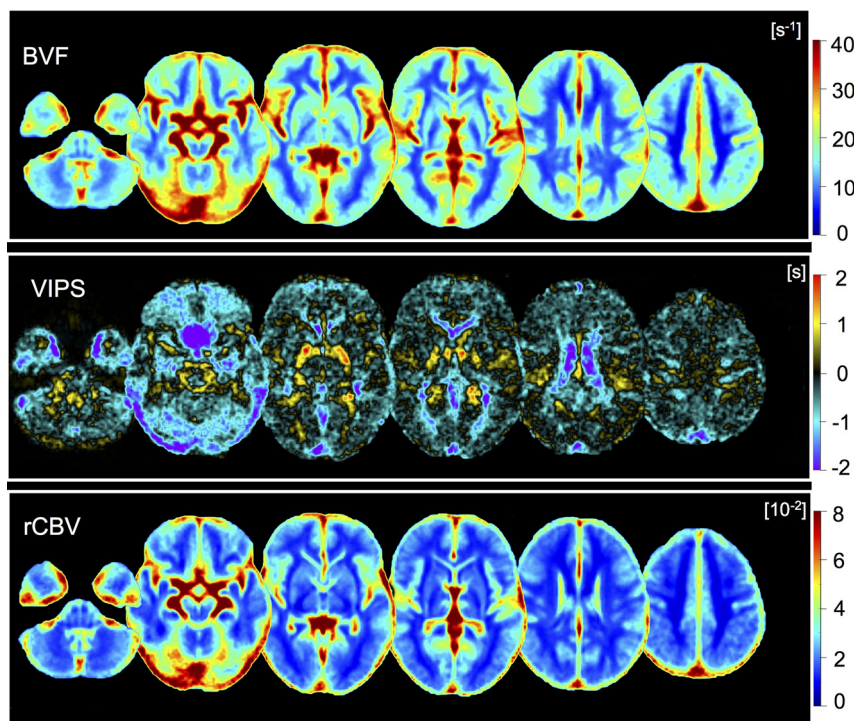
FIG 4. Parametric maps for CBV fraction, VIPS, and rCBV. Parameters BVF, VIPS, and rCBV are shown as spatially normalized, averaged axial parametric maps in MNI standard space as above. Because BVF identifies regions with increased blood volume, it is similar to rCBV with moderate correlations between both parameter values in the cGM and WM, respectively (Online Supplemental Data). The parameter VIPS is highly increased in the GP and thalamus (Table 2), as well as in parts of the WM along the pyramidal tracts.
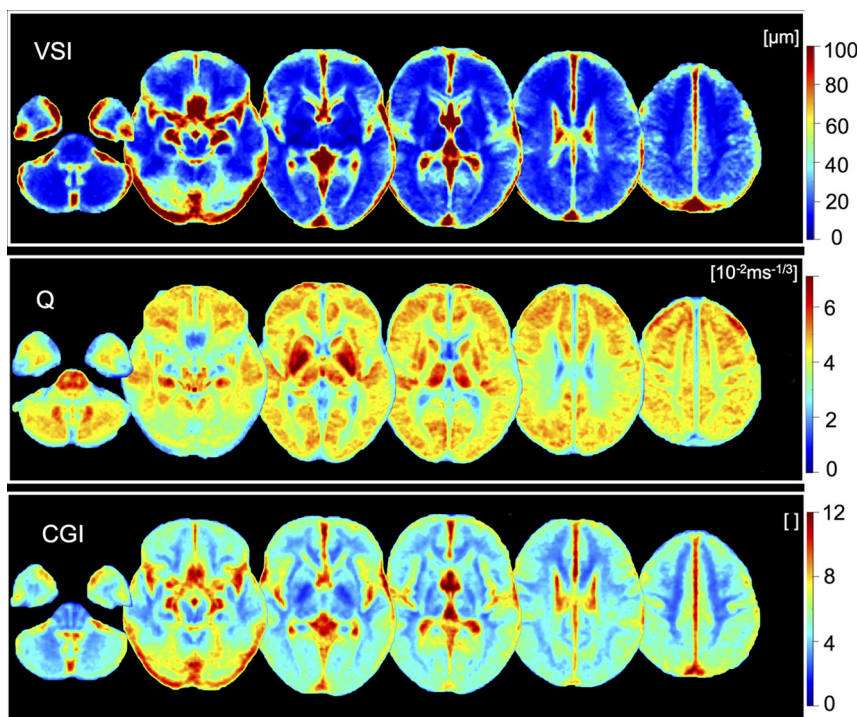
FIG 5. Color maps of VSI, microvessel density Q, and CGI. Parameters VSI, Q, and CGI are shown as spatially normalized, averaged axial parametric maps in MNI standard space as above. Parameters VSI and CGI indicate larger vessel calibers in the cGM compared with WM (Table 2). Microvessel density Q is increased in the lenticular nucleus (GP and putamen) and thalamus, compared with WM.

VTI). This effect was not observed for the other VAM parameters.

Correlation of VAM Parameters

Partial correlation analysis revealed a positive correlation among VTI, I, and VIPS for both cGM and WM VOIs, controlling for age and BMI (all $P < .001$) (Online Supplemental Data). Additionally, I and VTI were negatively correlated with parameters CGI, CBI, and BVF (all $P < .001$). rCBV was positively correlated with CGI, BVF, and VSI (all $P < .05$). The VSI was positively correlated with the CGI ($P < .001$) and negatively correlated with microvessel density Q ($P < .001$).

There was no significant correlation between structural parameters VTI and VSI or blood flow velocity indicators VIPS and rCBV.

DISCUSSION

To our knowledge, this is the first VAM study to comprehensively map cerebral microvasculature in healthy tissue for a large collective, using standardized 3D VOIs from whole-brain VAM scans.

The main findings of our study were the following: 1) that VAM finds distinct microvascular profiles in supratentorial brain structures, differentiating GM, WM, and basal ganglia vasculature; 2) that healthy brain tissue displays an overall predominance of venule- and capillary-like vessels; 3) that VAM parameters that make use of the vortex curve direction (I, VTI, and VIPS) are positively correlated, while parameters CGI, VSI, and BVF are positively correlated with rCBV.

Our analysis showed distinct patterns when comparing microvasculature properties for different neuroanatomic structures. cGM voxels contained vessels with larger calibers compared with WM, as measured with both CGI and VSI. Compared with WM, cGM vasculature contains a higher proportion and density of veins[24] that have larger radii than arteries.[25] In accordance with the study of Zhang et al,[7] our study showed an overall predominance of capillaries and venules in healthy brain tissue, as measured by negative values for VAM parameters I and VTI. Because VTI

Table 3: ICCs between 2 scans (*n* = 27)[a]

Parameter	ICC	95% CI	F	P
I	0.4895	[0.3814–0.5844]	2.9241	<.0001
VTI	0.3623	[0.2406–0.4727]	2.1337	<.0001
CBI	0.7297	[0.6591–0.7873]	6.5456	<.0001
BVF	0.7771	[0.7182–0.8250]	7.9463	<.0001
VIPS	0.5689	[0.4713–0.6527]	3.6274	<.0001
rCBV	0.9274	[0.9061–0.9440]	26.4302	<.0001
VSI	0.9163	[0.892–0.9353]	22.969	<.0001
Q	0.853	[0.8046–0.8890]	13.3324	<.0001
CGI	0.8109	[0.7598–0.8520]	9.5721	<.0001

[a] ICC estimates with 95% confidence intervals for each parameter and the *F* test for the hypothesis that ICC = 0. Mean values for 8 VOIs were compared between *n* = 27 individual subjects at 2 different time points (*n* = 216 values per time point).

values have been shown to correlate with vascular branching patterns,[26] more negative VTI values for cGM reflect an asymmetric vascular branching structure, as typically found in GM vasculature.[25] Additionally, cGM voxels had a higher BVF and higher rCBV than WM, supporting previous studies that showed higher CBV and CBF in GM.[27]

For subcortical GM nuclei, GM-like and WM-like microvascular phenotypes emerged: The microvasculature of the CN was structurally closer to the cGM, as found by similar values between the CN and cGM for CGI, VSI, and VTI, but a significant difference compared with WM. Vessel architecture parameters for the putamen, GP, and thalamus were more WM-like, as indicated by a significant difference from the cGM and CN, but not from WM, for the VTI. Intersubject variability in vessel size was highest in the CN. Because the basal ganglia are a predilection site for small-vessel disease and lacunar infarctions,[28] variation in vessel lumen might be an early sign of varying degrees of plaque deposition and media thickening, with potential applications for clinical diagnostics.

CBV, as measured by rCBV and BVF, differed significantly between the CN and cGM but not between the CN and the other subcortical nuclei. Similarly, the putamen did not differ from the GP in terms of CBV but by microstructural properties, such as CGI and microvessel density Q. This finding indicates that the basal ganglia share more similarities in functional than in structural properties of their vascular networks, potentially reflecting differences in embryology and development.[29]

The highest values for the CBF velocity indicator VIPS were measured in the GP, followed by the thalamus and putamen. While VIPS showed negative values for most examined VOIs, indicating again a dominance of slow-flowing, venous-like vessels in healthy tissue, our findings point toward a comparatively high density of fast-flowing vessels, such as arterioles, in the GP.[5,17] Additionally, microvessel density Q was highest in the GP, followed by the putamen and thalamus, consistent with histologic ex vivo findings.[30]

The similarity of the amygdala and hippocampus in VAM characteristics indicates similar microvascular profiles and potentially similar pathogenetic microvascular alterations, as already shown in the pathogenesis of epilepsy or neurodegeneration.[31,32]

In accordance with the study of Zhang et al,[7] parameters I, VTI, and VIPS that incorporated the vortex curve direction were positively correlated. Both I and VTI were negatively correlated with CGI, CBI, and BVF. Furthermore, the parameters CGI,

BVF, and VSI were positively correlated with rCBV. The VSI was positively correlated with the CGI and inversely correlated with microvessel density Q. In summary, only the combination of different VAM parameters was able to reveal the full microvascular profile of the analyzed structures in healthy tissue. It is, therefore, essential, to simultaneously quantify multiple VAM parameters.

Previous vessel architecture imaging studies[6,7] have reported data mainly from patients with high-grade gliomas after standard radiochemotherapy. However, there are short- and long-term effects of chemo- and radiation therapy on the cerebral microvasculature.[33,34] We present the first study that includes only the contralateral hemispheres from patients with stable low-grade (World Health Organization grades 1-2) lesions who underwent examinations without any prior radio- or chemotherapy. Given potential contrast agent adverse effects, such as retention in the brain,[35] we intentionally chose to use available data from clinical routine follow-ups of patients instead of a large healthy volunteer collective. Still, for a small fraction of patients with a specific low-grade brain tumor subtype, diffuse low-grade glioma, tumor recurrence patterns on the contralateral side have been observed, suggesting tumor cell migration.[36] However, no patient in this study showed suspect lesions in the healthy-termed hemisphere, thus suggesting that, at most, only a very small amount of cells may have migrated, which is not expected to have a relevant influence on microvascular properties within the observed MR imaging VOIs.

Not only microvascular architecture but also imaging parameters such as T2 and T2* vary depending on demographic factors such as age.[37] Our patient collective matched the average age and cardiovascular risk factor prevalence of the general German population. However, further research should also consider the effects of age and different cardiovascular risk factors on VAM parameter values.

Last, the reported reference values were obtained on a single site and single scanner. While no comparable whole-brain studies were available, our findings for WM voxels were within the ranges of values reported by previous studies[5,17,38] as well as histologic ex vivo studies. Nevertheless, future research should include multisite, multivendor parameter acquisitions.

Furthermore, analyses showed overall high test-retest reliability for VAM parameter values. Outliers were rare but found mainly for small VOIs for signed parameters I and VTI, indicating the need for caution when analyzing and interpreting results from VOIs below a certain volume (in this case, the GP and amygdala) for these parameters.

We chose to report mean values for standardized VOIs from an established, publicly available neuroanatomical atlas, the AAL3,[19] to facilitate the use of our reference values. While all VOIs were checked visually, a certain overlap with other anatomic structures could not be entirely avoided. Additionally, we compared MR images that were macroscopically stable and unchanged on T1 imaging but might have had changes on the microvascular level; therefore, higher intrasubject variability might reflect microscopic changes that had not been detected by traditional MR imaging sequences. Future research should include test-retest studies at fixed time intervals.

CONCLUSIONS

This study provides a whole-brain atlas of VAM reference values and shows that VAM parameters representing microvascular arrangements differ between the cGM and basal ganglia. This difference is of particular importance with regard to future studies on the impact of cortical and basal ganglia microvasculature in patients with neurodegenerative and neurovascular disorders.

Disclosure forms provided by the authors are available with the full text and PDF of this article at www.ajnr.org.

REFERENCES

1. Hahn A, Bode J, Krüwel T, et al. **Glioblastoma multiforme restructures the topological connectivity of cerebrovascular networks**. *Sci Rep* 2019;9:11757 CrossRef Medline
2. Granger DN, Rodrigues SF, Yildirim A, et al. **Microvascular responses to cardiovascular risk factors**. *Microcirculation* 2010;17:192–205 CrossRef Medline
3. Wardlaw JM, Smith C, Dichgans M. **Small vessel disease: mechanisms and clinical implications.** *Lancet Neurol* 2019;18:684–96 CrossRef Medline
4. Hahn A, Bode J, Krüwel T, et al. **Gibbs point field model quantifies disorder in microvasculature of U87-glioblastoma**. *J Theor Biol* 2020;494:110230 CrossRef Medline
5. Emblem KE, Mouridsen K, Bjornerud A, et al. **Vessel architectural imaging identifies cancer patient responders to anti-angiogenic therapy**. *Nat Med* 2013;19:1178–83 CrossRef Medline
6. Kim M, Park JE, Emblem K, et al. **Vessel type determined by vessel architectural imaging improves differentiation between early tumor progression and pseudoprogression in glioblastoma**. *AJNR Am J Neuroradiol* 2021;42:663–70 CrossRef Medline
7. Zhang K, Yun SD, Triphan SM, et al. **Vessel architecture imaging using multiband gradient-echo/spin-echo EPI**. *PLoS One* 2019;14: e0220939 CrossRef Medline
8. Kiselev VG, Strecker R, Ziyeh S, et al. **Vessel size imaging in humans**. *Magn Reson Med* 2005;53:553–63 CrossRef Medline
9. Buschle LR, Ziener CH, Zhang K, et al. **Vessel radius mapping in an extended model of transverse relaxation**. *MAGMA* 2018;31:531–51 CrossRef Medline
10. Stadlbauer A, Zimmermann M, Oberndorfer S, et al. **Vascular hysteresis loops and vascular architecture mapping in patients with glioblastoma treated with antiangiogenic therapy**. *Sci Rep* 2017;7:8508 CrossRef Medline
11. Kim M, Park JE, Yoon SK, et al. **Vessel size and perfusion-derived vascular habitat refines prediction of treatment failure to bevacizumab in recurrent glioblastomas: validation in a prospective cohort**. *Eur Radiol* 2023;33:4475–85 CrossRef Medline
12. Choi HI, Ryu CW, Kim S, et al. **Changes in microvascular morphology in subcortical vascular dementia: a study of vessel size magnetic resonance imaging**. *Front Neurol* 2020;11:545450 CrossRef Medline
13. Xu C, Schmidt WU, Villringer K, et al. **Vessel size imaging reveals pathological changes of microvessel density and size in acute ischemia**. *J Cereb Blood Flow Metab* 2011;31:1687–95 CrossRef Medline
14. Boxerman JL, Schmainda KM, Weisskoff RM. **Relative cerebral blood volume maps corrected for contrast agent extravasation significantly correlate with glioma tumor grade, whereas uncorrected maps do not**. *AJNR Am J Neuroradiol* 2006;27:859–67 Medline
15. Rausch M, Scheffler K, Rudin M, et al. **Analysis of input functions from different arterial branches with gamma variate functions and cluster analysis for quantitative blood volume measurements**. *Magn Reson Imaging* 2000;18:1235–43 CrossRef Medline
16. Xu C, Kiselev VG, Möller HE, et al. **Dynamic hysteresis between gradient echo and spin echo attenuations in dynamic susceptibility contrast imaging**. *Magn Reson Med* 2013;69:981–91 CrossRef Medline
17. Stadlbauer A, Zimmermann M, Heinz G, et al. **Magnetic resonance imaging biomarkers for clinical routine assessment of microvascular architecture in glioma**. *J Cereb Blood Flow Metab* 2017;37:632–43 CrossRef Medline
18. D'Agostino E, Maes F, Vandermeulen D, et al. **A viscous fluid model for multimodal non-rigid image registration using mutual information**. *Med Image Anal* 2003;7:565–75 CrossRef Medline
19. Rolls ET, Huang CC, Lin CP, et al. **Automated anatomical labelling atlas 3**. *Neuroimage* 2020;206:116189 CrossRef Medline
20. Zhang Y, Brady M, Smith S. **Segmentation of brain MR images through a hidden Markov random field model and the expectation-maximization algorithm**. *IEEE Trans Med Imaging* 2001;20:45–57 CrossRef Medline
21. Wenz F, Rempp K, Brix G, et al. **Age dependency of the regional cerebral blood volume (rCBV) measured with dynamic susceptibility contrast MR imaging (DSC)**. *Magn Reson Imaging* 1996;14:157–62 CrossRef Medline
22. Koo TK, Li MY. **A guideline of selecting and reporting intraclass correlation coefficients for reliability research**. *J Chiropr Med* 2016;15:155–63 CrossRef Medline
23. Heidemann C, Scheidt-Nave C, Beyer AK, et al. **Health situation of adults in Germany: results from GEDA 2019/2020-EHIS**. *J Health Monit* 2021;6:3–35 CrossRef Medline
24. Bernier M, Cunnane SC, Whittingstall K. **The morphology of the human cerebrovascular system**. *Hum Brain Mapp* 2018;39:4962–75 CrossRef Medline
25. Reina-De La Torre F, Rodriguez-Baeza A, Sahuquillo-Barris J. **Morphological characteristics and distribution pattern of the arterial vessels in human cerebral cortex: a scanning electron microscope study**. *Anat Rec* 1998;251:87–96 CrossRef Medline
26. Digernes I, Bjørnerud A, Vatnehol SA, et al. **A theoretical framework for determining cerebral vascular function and heterogeneity from dynamic susceptibility contrast MRI**. *J Cereb Blood Flow Metab* 2017;37:2237–48 CrossRef Medline
27. Helenius J, Soinne L, Perkiö J, et al. **Diffusion-weighted MR imaging in normal human brains in various age groups**. *AJNR Am J Neuroradiol* 2002;23:194–99 Medline
28. Caplan LR. **Lacunar infarction and small vessel disease: pathology and pathophysiology.** *J Stroke* 2015;17:2–6 CrossRef Medline
29. Wolfram-Gabel R, Maillot C. **Vascular networks of the nucleus lentiformis.** *Surg Radiol Anat* 1994;16:373–77 CrossRef Medline
30. Kubíková T, Kochová P, Tomášek P, et al. **Numerical and length densities of microvessels in the human brain: correlation with preferential orientation of microvessels in the cerebral cortex, subcortical grey matter and white matter, pons and cerebellum**. *J Chem Neuroanat* 2018;88:22–32
31. Manna A, Piras F, Caltagirone C, et al. **Left hippocampus-amygdala complex macro- and microstructural variation is associated with BDNF plasma levels in healthy elderly individuals**. *Brain Behav* 2015;5:e00334 CrossRef Medline
32. van Lanen RH, Melchers S, Hoogland G, et al. **Microvascular changes associated with epilepsy: a narrative review**. *J Cereb Blood Flow Metab* 2021;41:2492–509 CrossRef Medline
33. Soultati A, Mountzios G, Avgerinou C, et al. **Endothelial vascular toxicity from chemotherapeutic agents: preclinical evidence and clinical implications**. *Cancer Treat Rev* 2012;38:473–83 CrossRef Medline
34. Bálentová S, Adamkov M. **Pathological changes in the central nervous system following exposure to ionizing radiation**. *Physiol Res* 2020;69:389–404 CrossRef Medline

35. Radbruch A, Weberling LD, Kieslich PJ, et al. **Gadolinium retention in the dentate nucleus and globus pallidus is dependent on the class of contrast agent.** *Radiology* 2015;275:783–91 CrossRef Medline

36. Fukuya Y, Ikuta S, Maruyama T, et al. **Tumor recurrence patterns after surgical resection of intracranial low-grade gliomas.** *J Neurooncol* 2019;144:519–28 CrossRef Medline

37. Siemonsen S, Finsterbusch J, Matschke J, et al. **Age-dependent normal values of T2* and T2' in brain parenchyma.** *AJNR Am J Neuroradiol* 2008;29:950–55 CrossRef Medline

38. Jensen JH, Lu H, Inglese M. **Microvessel density estimation in the human brain by means of dynamic contrast-enhanced echo-planar imaging.** *Magn Reson Med* 2006;56:1145–50 CrossRef Medline